Shock-induced plasticity in nanocrystalline iron: Large-scale molecular dynamics simulations

Hoang-Thien Luu,[1] Ramon J. Ravelo,[2] Martin Rudolph,[3] Eduardo M. Bringa,[4] Timothy C. Germann,[5]
David Rafaja [3] and Nina Gunkelmann [1,*]

[1]*Institute of Applied Mechanics, Clausthal University of Applied Technology,
Arnold-Sommerfeld-Straße, D-38678 Clausthal-Zellerfeld, Germany*
[2]*Physics Department and Materials Research Institute, University of Texas, El Paso, Texas 79968, USA*
[3]*Institute of Materials Science, TU Bergakademie Freiberg, Gustav-Zeuner-Straße 5, D-09599 Freiberg, Germany*
[4]*CONICET and Faculty of Engineering, University of Mendoza, Mendoza 5500, Argentina*
[5]*Theoretical Division, Los Alamos National Laboratory, Los Alamos, New Mexico 87545, USA*

Large-scale nonequilibrium molecular dynamics (MD) simulations of shock waves in nanocrystalline iron show evidence of plasticity before the polymorphic transformation takes place. The atomistic structure in the shock direction shows an elastic precursor, plastic deformation, and shock-induced phase transformation from bcc to hcp iron. In this Rapid Communication, large-scale MD models show that the shock response of iron is highly related to the ramp time of the applied shocks. For long ramp times we observe significant plastic relaxation and formation of microstructure defects. Pressure-induced phase transformations in iron are accompanied by stress relaxation achieving almost fully relaxed three-dimensional hydrostatic final states. The evolution of the stress relaxation is in agreement with theory and experiments. Analysis of the x-ray diffraction patterns calculated from the atomistic structure using the Debye equation revealed pronounced anisotropy of the line broadening that is caused by stacking faults in hcp Fe and by dislocations in bcc Fe.

In-depth knowledge of the crystal structure and its changes under high pressures plays a crucial role in understanding the mechanical properties of heavily deformed metallic materials. Structure changes in iron are of particular importance, because iron is one of the most common metals and undergoes several phase transitions at high temperatures and high pressure. For these reasons, the study of iron under extreme conditions is essential not only for industry but also for geological and astronomical applications. Iron transforms from the body-centered-cubic crystal structure (bcc/α) Fe to face-centered-cubic (fcc/γ) Fe at high temperatures and hexagonal-close-packed (hcp/ε) Fe at high pressures [1,2].

The pressure-induced phase transformation in iron has been attracting considerable interest since the hcp phase has been discovered by wave-profile measurements [1]. Strong-shock experiments performed on polycrystalline iron [1,3] demonstrated that the free surface velocity profile can be divided into three regions consisting of an elastic wave, a plastic wave, and a diffusionless phase transformation. Recently, this has been confirmed by high-quality x-ray diffraction data of the subnanosecond dynamics of laser-shocked polycrystalline iron [4]. Continuous models are able to describe the polymorphism of iron under high pressure [5,6]. These models emphasize the major role of plastic deformation on the morphological evolution. In shock experiments, timescales are sufficiently short, thus large-scale molecular dynamics

(MD) simulations can help in understanding the deformation processes and in improving mesoscale models.

Large-scale molecular dynamics simulations were already used to study shock waves in iron single crystals [7,8], bicrystals [9], and polycrystals [10–12]. For single crystals, it was shown that the phase transformation proceeds differently in different crystallographic directions [8]. However, large-scale MD simulations of nanocrystalline iron by Kadau *et al.* [10] showed no evidence of dislocation activity in the bcc phase before the α/ε phase transformation. The Voter [13] potential used in their study shows, in contrast to experiments, a significant fraction of fcc under high pressure. Gunkelmann *et al.* [12] performed MD simulations of piston-driven shock waves using a modified Ackland potential [11] and found that the shocked material exhibits a dominant hcp phase. However, due to the limited computing power, the authors were not able to carry out a detailed study of the plastic deformation including the analysis of dislocation density and three-dimensional (3D) plastic relaxation. Also, the relationship between the shear stress and the phase fraction of the two phases fcc and hcp was not identified.

Caspersen *et al.* [14] used a multiscale model containing a quantum-mechanics-based multiwell energy function counting for the bcc and hcp phases of Fe to reveal the essential role of the shear stress in the α/ε transition. The result from Ref. [14] is in agreement with the finding of Shao *et al.* [15] showing the relationships between shear deformations and hcp and fcc fractions during the martensitic transformation process in iron under high pressure. Nonequilibrium MD (NEMD) simulations of shock waves in a 1-μm-long Cu fcc single crystal [16] have shown that the stress upon uniaxial

*nina.gunkelmann@tu-clausthal.de; https://www.itm.tu-clausthal.de.

compression relaxes to a nearly hydrostatic state where the dislocation velocity drops to zero. Their result is in agreement with x-ray diffraction experiments [17,18]. The shear stress and dislocation density reach a maximum simultaneously, and the ramp time significantly influences the lateral relaxation [16]. So far, however, little is known about this phenomenon in iron.

The aim of this Rapid Communication is to unravel plastic relaxations at the subnanosecond timescale in shock-compressed iron by large-scale NEMD simulations of shock wave propagation through 0.89-μm-thick nanocrystalline iron. The sample consisting of 265.5 million atoms and 396 grains with a mean diameter of 20 nm was relaxed at 800 K, followed by an annealing procedure of 100 ps to the desired temperature of 300 K at zero pressure. The momentum mirror method [19] was adopted to simulate the shock. A piston with a velocity of 0.75 km/s was applied to generate the shock wave using two different ramp times of 20 and 50 ps. The piston velocity was increased linearly from zero to the desired value during this time. Periodic boundary conditions were applied in the x and y directions of the sample, while free boundaries were assumed in the shock direction (along the z axis). The simulations were carried out by using the scalable parallel short-range molecular dynamics (SPaSM) code [20], and the Ackland potential [11] featuring the $\alpha \rightarrow \varepsilon$ phase transformation at a pressure of 13.75 GPa.

The centrosymmetry analysis [21] was used to detect crystallographic defects by identifying disordered local crystal structures, such as line and planar defects. Snapshots showing noncentrosymmetric atoms for 20- and 50-ps ramp simulations are shown in Figs. 1(a) and 1(b), respectively. Both cases display clearly three regions: the defective structure on the left (new phases and grain boundaries), a short period of the transition area, and bcc grains on the right. For the 20-ps ramp, the new phases (disordered or close-packed crystal structure) extend over a larger area than for 50 ps. From Figs. 1(c) and 1(d), we observe that the effective grain size is much smaller in the hcp due to planar faults. The longitudinal pressure P_{zz} and the shear stress P_{shear} in Fig. 1(e) provide information on the response of the sample behind the shock front. For both simulations, the shock velocity measured from the time difference of the shock front is 5.5 km/s, and the longitudinal stress in the daughter phases is 31 GPa, which is in agreement with MD results by Kadau *et al.* [10] and close to experimental data [22].

The pressure and stress profiles show three stages of material response during the passage of the shock wave from left to right (Fig. 1). The colored areas on top of the black curve and below the blue curve represent these three distinct states for 20- and 50-ps ramp simulations (elastic wave in blue, plasticity in green, and transition period in yellow). These waves are defined by sudden changes in the stress profile dividing the material into three sections, the so-called three-wave structure of the shock [12]. There are only a few theoretical and experimental studies which evaluate the shear stress in iron under shock loading. By using large-scale MD simulations of shock waves though copper, Bringa *et al.* [16] reported a rapid increase of the shear stress before the nucleation of dislocations and lattice relaxations at a subnanosecond timescale.
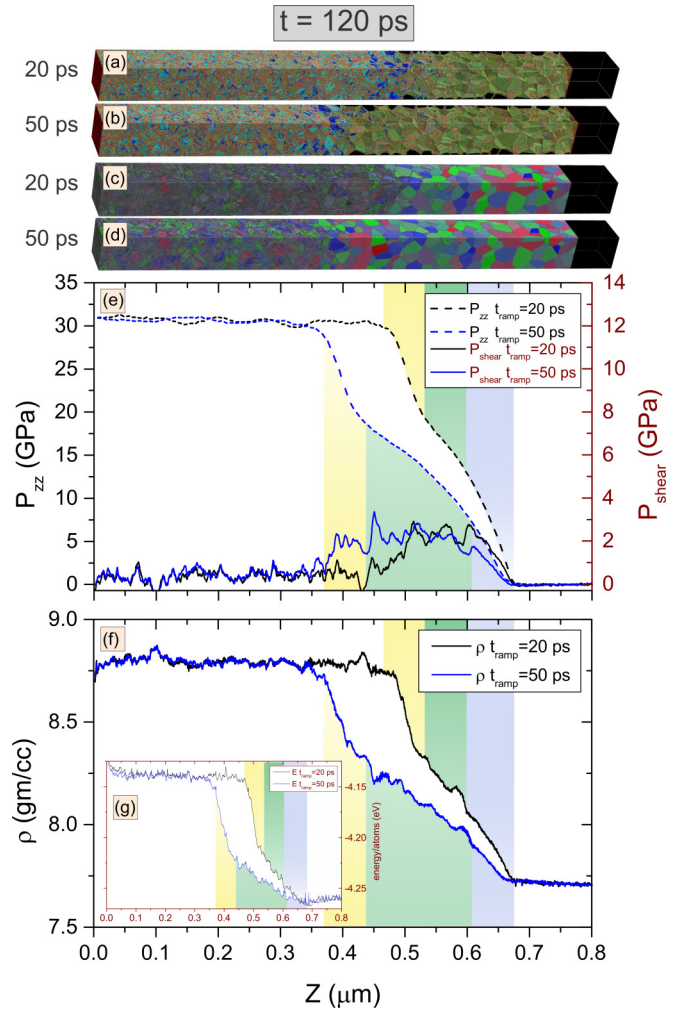

FIG. 1. Response of nanocrystalline iron under shock loading after 120 ps. In snapshots of the sample with the ramp times (a) t_{ramp} = 20 ps and (b) 50 ps, noncentrosymmetric atoms are highlighted; the black area is the background of the simulation domain. In (c) and (d), the grains are colored according to their local orientation with respect to the shock direction. (e) shows the longitudinal pressure and shear stress along the shock wave direction, $P_{shear} = \frac{1}{2}[P_{zz} - \frac{1}{2}(P_{xx} + P_{yy})]$. Elastic, plastic, and transition periods are plotted as blue, green, and yellow areas. For the 20-ps ramp, these areas are shown above the black dashed line, and for the 50-ps simulation below the blue dashed line. (f) Density along the sample; the distribution of energies is embedded in (g). The energy per atom and transition stages of both simulations are almost identical except at the beginning of the phase transition. Here, the energy per atom for the 50-ps ramp is 0.01 eV less than for the other case.

Statistical analysis of the atomic positions obtained from the MD simulation was done through the calculation of the x-ray diffraction (XRD) patterns and their analysis. For the calculation, a routine [23–25] was used that is based on the Debye scattering equation [26]. The sample regions, exposed to a pressure of about 30 GPa, contained hcp Fe as the dominant phase (two bottom curves in Fig. 2). In the part of the sample which was exposed to pressures between 30 and 20 GPa, a mixture of different fractions of hcp and bcc was identified (three upper curves in Fig. 2). For hcp Fe, the
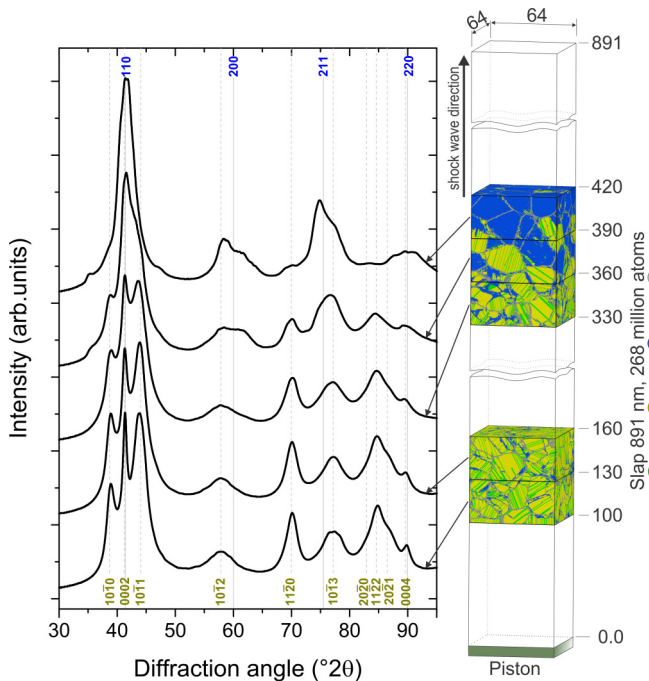
FIG. 2. XRD patterns calculated using the Debye equation [26] for slabs cut from the sample displayed in Fig. 1(d). The thickness of the slabs in the z direction was 30 nm; their starting positions were 100, 130, 330, 360, and 390 nm (from bottom to top). Vertical lines indicate positions of the diffraction lines from hcp Fe (dashed lines) and bcc Fe (solid lines). Diffraction indices are attached. The x-ray wavelength used for calculation of the XRD patterns was 0.140 891 nm. The intensities are plotted in a square-root scale.

Rietveld analysis of the XRD patterns using MAUD [27] revealed lattice parameters $a = 0.245\,55(2)$ nm and $c = 0.399\,26(5)$ nm (in the 30 GPa region) and $a = 0.246\,19(9)$ nm and $c = 0.393\,88(8)$ nm (in the 20–25 GPa region). The lattice parameter a decreases with increasing pressure as expected. According to Refs. [28,29], the refined values correspond to hydrostatic pressures of approximately 17 and 14 GPa. The lattice parameter c shows an opposite trend. This is related to the change of the c/a ratio from 1.60 at 20–25 GPa to 1.63 at 30 GPa that accompanies marten-sitic phase transformations and interactions between adjacent phases [30]. The value of $c/a = 1.603$ is typically reported for ε-Fe [28,29], where $c/a = 2\sqrt{2}/\sqrt{3} = 1.633$ corresponds to a pseudocubic hcp structure [29].

In both bcc and hcp, the line broadening depends strongly on diffraction indices. In hcp, this anisotropy of the line broadening indicates that the main microstructure defects are stacking faults (SFs) on the lattice planes $\{0001\}_{hcp}$, which broaden the diffraction lines with $h - k = 3n \pm 1$ (n integer) increasingly with increasing diffraction index l [31,32]. The broadening of diffraction lines $11\bar{2}0$ and $11\bar{2}2$, which are not affected by these SFs, stems from dislocations. A relatively small broadening of the hcp diffraction lines 002 and 004 is caused by the crystallographic coherence of the bcc and hcp structures having the orientation relationship $\{110\}_{bcc} \parallel \{0001\}_{hcp}$. This coherence leads to a "narrowing" of the corresponding diffraction lines, because XRD does

not recognize the $(110)_{bcc}/(0001)_{hcp}$ interface as a crystallite boundary. Consequently, the hcp crystallites appear larger in the [0001] direction than in reality [33]. Concurrently, the crystallographic coherence between bcc and hcp implies a heteroepitaxy at the $\{110\}_{bcc}/\{0001\}_{hcp}$ interfaces leading to a distortion of the bcc elementary cell that is visible in the shift of the bcc diffraction lines 200 ($2\theta = 60°$) and 211 ($2\theta = 75.5°$) in opposite directions from the expected positions. The crystallographic anisotropy of the line broadening in bcc Fe indicates the presence of dislocations. The microstructure observed agrees with recent laser-shock experiments on single and polycrystalline iron [4,34].

From Fig. 1(e), we observe an increase of the shear stress as expected, followed by fluctuations around a shear stress of 2.5 GPa, before it decreases to a small value. This is evidence of hydrostatic compression because fully relaxed 3D states are characterized by roughly zero shear stress. In the simulated XRD patterns, the residual hydrostatic compression of the crystal lattice is evidenced by the stabilization of hcp Fe and by the observed dependence of the lattice parameter a_{hcp} on the pressure [cf. Fig. 1(e)]. The shear stress facilitates the phase transition $\alpha \rightarrow \varepsilon$ and the formation of microstructure defects.

The elastic limit and the onset of the phase transformation highly depend on the ramp time. The longitudinal pressure P_{zz} shows that the elastic limit of the 50-ps ramp reaches a pressure of 6.94 GPa after 6.6 ps behind the shock front. The elastic limit for the 20-ps ramp simulation is 5.81 GPa higher than for the 50-ps ramp, where the period of plasticity is 2.5 times longer than for the 20-ps ramp. The onset of the phase transformation increases with increasing ramp time. The shear stress amplitude for both simulations is comparable. Following the peak shear stress we observe a sharp plunge at the beginning of the transition process. The longitudinal pressure P_{zz} decreases sharply during the phase transformation in iron. Our result supports the finding of Amadou *et al.* [35] showing that for ramp compressed samples, the shear stress plays a significant role for the phase transformation in iron single crystals. Our finding is also in agreement with comparable NEMD simulations for fcc materials [16]. At the beginning and at the end of the transition, the density of iron in the two simulations is identical, but the energy of the longer ramp time is 0.01 eV lower at the transition as shown in Figs. 1(f) and 1(g).

A snapshot of the local crystal structure at the transition area of the 50-ps ramp simulation shown in Fig. 3(a) provides closer insight into the transition zone. During the plastic deformation, the hcp phase nucleates at the grain boundaries. In some grains, many hcp clusters form and extend, until they encounter other dense clusters or grain boundaries. In other regions, the hcp clusters stretch across the whole parent grain. In accordance with Ref. [37], the centrosymmetry analysis interprets SFs in hcp as laths of the fcc phase [Fig. 3(a)].

In Fig. 3(b), a slice of thickness 7 nm in the plastically deformed region is displayed. We observe straight screw dislocations nucleating at grain boundaries and crossing the grains. In addition, several dislocation loops and vacancies appear. Dislocations in Fig. 3(b) are detected by the dislocation extraction algorithm [38] implemented in the open visualization tool (OVITO) [36]. The algorithm detects many
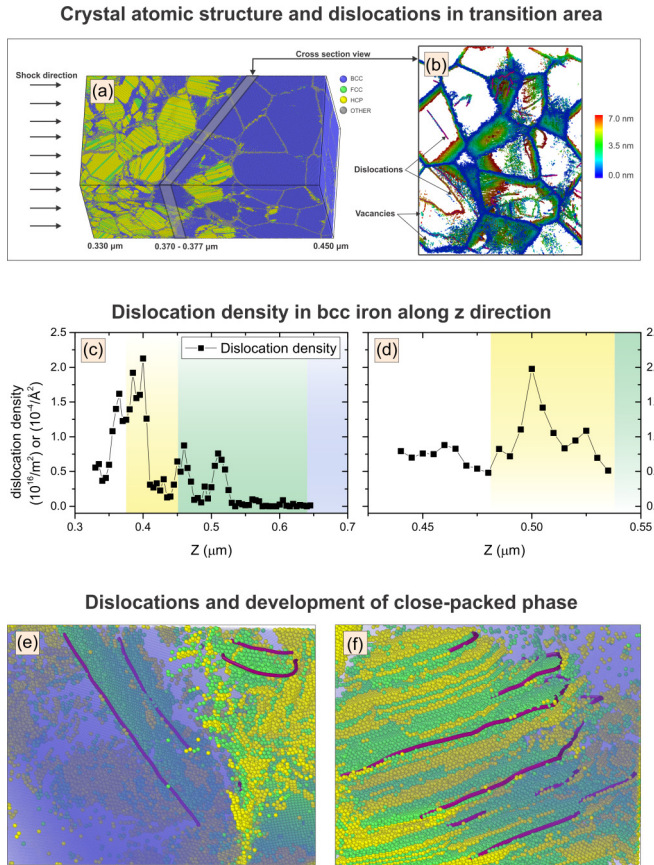
Crystal atomic structure and dislocations in transition area

Dislocation density in bcc iron along z direction

Dislocations and development of close-packed phase

FIG. 3. Phases and microstructure defects in the transition area at 120 ps. (a) Snapshot of a simulation with t_{ramp} = 50 ps. Atoms are colored according to the local crystal structure—blue: bcc; green: fcc; yellow: hcp; gray: disordered atoms. (b) A 7-nm-thick slice of the sample showing the propagation of dislocations of type $\frac{1}{2}\langle 111 \rangle$. Only atoms of the grain boundaries and disordered atoms are shown. The color code indicates the depth of the atoms. The visualization has been done by OVITO [36]. (c) and (d) Dislocation densities for a ramp time t_{ramp} of 50 and 20 ps (left and right). Only dislocation segments which are generated by the shock wave are used to calculate the dislocation density. Background color: Blue, green, and yellow represent elastic, plastic, and transition periods of the sample. (e) and (f) Snapshots of the transition area where dislocations with proceeding laths of the fcc phase are shown.

types of dislocations at the atomistic scale, but it also detects a large number of dislocation segments as spiderlike dislocation networks belonging to the initial grain boundary structure [11]. In this work, only dislocations which were formed in the bulk during shock propagation are selected to calculate the dislocation density, while the dislocations at the grain boundaries were removed.

Experiments [39,40] proved that dislocations are generated behind the shock front in both fcc and bcc. The relaxation during the plastic response of the material is associated with dislocation kinetics [40]. Two diagnostic techniques [41], transmission electron microscopy and *in situ* x-ray diffraction, are used to analyze the plastic response during hydrostatic compression of iron single crystals. The experiments disclosed a high dislocation density in the parent material. In agreement with experiments [41], Figs. 3(c) and 3(d) give

high dislocation densities in bcc along the samples for 20- and 50-ps ramp simulations. Unfortunately, there is no theory predicting how dislocations evolve under the rapid rise of shear stress in shock waves. This information can only be obtained by MD simulations.

The dislocation density reaches nearly 2×10^{16} m^{-2} for both simulations, which is high for a small grain size of 20 nm. The nucleation of dislocations starts at grain boundaries at the beginning of the plastic response, and is followed by their pileup. In some grains, we observe strong dislocation activation. The dislocation pile-up at around 120 nm behind the shock front results in two peaks in the dislocation density during the plastic period of the 50-ps ramp simulation [Fig. 3(c)]. Glide planes of these dislocations are parallel to each other as shown in Figs. 3(e) and 3(f). In the parent (bcc) phase, most of the dislocation segments belong to the Burgers vector family of $\frac{1}{2}\langle 111 \rangle$.

The local crystal structures and dislocations in the sample at several picoseconds, 14.5 ps for the 20-ps ramp and 23.5 ps for the 50-ps ramp, after the passage of the shock front demonstrate the mobility of dislocations in a high-density environment. The volume ratio V/V_0 varies from 0.93 to 0.87. The movement of dislocations is correlated with the formation of hcp as shown in Figs. 3(e) and 3(f).

In conclusion, this Rapid Communication has examined the nature of nanocrystalline iron under strong shock waves on a subnanosecond timescale. The findings clearly indicate that the plasticity interval increases linearly with increasing ramp time. During the elastic wave, the shear stress is increasing and the high longitudinal and shear stresses initiate nucleation and pileup of dislocations. The peak shear stress and dislocation density are identical for 20- and 50-ps ramp simulations. The propagation of the hcp phase results in the reduction of shear stress leading to quasihydrostatic compression. The increase of the hcp phase fraction behind the shock front is evidence of the stability of hcp under strong shock compression. The mobility of dislocations in hcp Fe is highly related to the formation of SFs.

Kadau *et al.* [10] emphasized that the shock sample has to be long enough in order to be able to observe the entire inelastic response of the nanocrystalline structure and to capture the relaxation process from uniaxial or elastic compression to quasihydrostatic compression. Therefore, large-scale shock simulations as presented here are necessary to understand the plastic response of shock-loaded iron to explore different regimes of materials dynamics at extreme conditions. Due to this massive scale approach structural features at the transformation can be understood in more detail and we clearly observe 3D plastic relaxation. The simulated x-ray results are important for the design of shock experiments and they play a crucial role in the evaluation of MD simulations applying an embedded atom method (EAM) potential and in their comparison with the results of diffraction experiments.

Future simulations will cover the recovery of samples through shock release. Wang *et al.* [42] revealed a significant recovery of the bcc grains and observed significant twinning changing the microstructure of the samples. Simulations of homogeneous uniaxial compression and recovery using our potential have shown that the phase transformation helps to drive twinning [43]. This might be different

in nonequilibrium MD shock recovery simulations of nanocrystals, where the transient wave profile might change the unloaded microstructure.

[1] D. Bancroft, E. L. Peterson, and S. Minshall, J. Appl. Phys. **27**, 291 (1956).

[2] J. C. Jamieson and A. W. Lawson, J. Appl. Phys. **33**, 776 (1962).

[3] L. M. Barker and R. E. Hollenbach, J. Appl. Phys. **45**, 4872 (1974).

[4] H. Hwang, E. Galtier, H. Cynn, I. Eom, S. H. Chun, Y. Bang, G. C. Hwang, J. Choi, T. Kim, M. Kong, S. Kwon, K. Kang, H. J. Lee, C. Park, J. I. Lee, Y. Lee, W. Yang, S.-H. Shim, T. Vogt, S. Kim *et al.*, Sci. Adv. **6**, eaaz5132 (2020).

[5] A. Vattré and C. Denoual, J. Mech. Phys. Solids **92**, 1 (2016).

[6] A. Vattré and C. Denoual, J. Mech. Phys. Solids **131**, 387 (2019).

[7] K. Kadau, T. C. Germann, P. S. Lomdahl, and B. L. Holian, Science **296**, 1681 (2002).

[8] K. Kadau, T. C. Germann, P. S. Lomdahl, and B. L. Holian, Phys. Rev. B **72**, 064120 (2005).

[9] X. Zhang, J. Chen, W. Hu, W. Zhu, S. Xiao, H. Deng, and M. Cai, J. Appl. Phys. **126**, 045901 (2019).

[10] K. Kadau, T. C. Germann, P. S. Lomdahl, R. C. Albers, J. S. Wark, A. Higginbotham, and B. L. Holian, Phys. Rev. Lett. **98**, 135701 (2007).

[11] N. Gunkelmann, E. M. Bringa, K. Kang, G. J. Ackland, C. J. Ruestes, and H. M. Urbassek, Phys. Rev. B **86**, 144111 (2012).

[12] N. Gunkelmann, E. M. Bringa, D. R. Tramontina, C. J. Ruestes, M. J. Suggit, A. Higginbotham, J. S. Wark, and H. M. Urbassek, Phys. Rev. B **89**, 140102(R) (2014).

[13] R. J. Harrison, A. F. Voter, and S. P. Chen, in *Atomistic Simulation of Materials: Beyond Pair Potentials*, edited by V. Vitek and D. J. Srolovitz (Plenum, New York, 1994), pp. 281–286.

[14] K. J. Caspersen, A. Lew, M. Ortiz, and E. A. Carter, Phys. Rev. Lett. **93**, 115501 (2004).

[15] J.-L. Shao, P. Wang, F.-G. Zhang, and A.-M. He, Sci. Rep. **8**, 7650 (2018).

[16] E. M. Bringa, K. Rosolankova, R. E. Rudd, B. A. Remington, J. S. Wark, M. Duchaineau, D. H. Kalantar, J. Hawreliak, and J. Belak, Nat. Mater. **5**, 805 (2006).

[17] A. Loveridge-Smith, A. Allen, J. Belak, T. Boehly, A. Hauer, B. Holian, D. Kalantar, G. Kyrala, R. W. Lee, P. Lomdahl, M. A. Meyers, D. Paisley, S. Pollaine, B. Remington, D. C. Swift, S. Weber, and J. S. Wark, Phys. Rev. Lett. **86**, 2349 (2001).

[18] D. Milathianaki, S. Boutet, G. J. Williams, A. Higginbotham, D. Ratner, A. E. Gleason, M. Messerschmidt, M. M. Seibert, D. C. Swift, P. Hering, J. Robinson, W. E. White, and J. S. Wark, Science **342**, 220 (2013).

[19] B. L. Holian and P. S. Lomdahl, Science **280**, 2085 (1998).

[20] D. Beazley and P. Lomdahl, Parallel Comput. **20**, 173 (1994).

[21] C. L. Kelchner, S. J. Plimpton, and J. C. Hamilton, Phys. Rev. B **58**, 11085 (1998).

[22] J. M. Brown, J. N. Fritz, and R. S. Hixson, J. Appl. Phys. **88**, 5496 (2000).

[23] M. Dopita, M. Rudolph, A. Salomon, M. Emmel, C. G. Aneziris, and D. Rafaja, Adv. Eng. Mater. **15**, 1280 (2013).

[24] M. Rudolph, M. Motylenko, and D. Rafaja, IUCrJ **6**, 116 (2019).

[25] M. Rudolph, cuDebye v1.5, 2018, https://github.com/Martin-Rudolph/cuDebye.

[26] P. Debye, Ann. Phys. **351**, 809 (1915).

[27] M. Ferrari and L. Lutterotti, J. Appl. Phys. **76**, 7246 (1994).

[28] P. M. Giles, M. H. Longenbach, and A. R. Marder, J. Appl. Phys. **42**, 4290 (1971).

[29] H. Mao, W. A. Bassett, and T. Takahashi, J. Appl. Phys. **38**, 272 (1967).

[30] S. Ackermann, S. Martin, M. R. Schwarz, C. Schimpf, D. Kulawinski, C. Lathe, S. Henkel, D. Rafaja, H. Biermann, and A. Weidner, Metall. Mater. Trans. A **47**, 95 (2016).

[31] B. E. Warren, *X-ray Diffraction* (Dover, New York, 1990), pp. 116–117, 262–275, 298–314.

[32] C. Schimpf, M. Motylenko, and D. Rafaja, Mater. Charact. **86**, 190 (2013).

[33] D. Rafaja, V. Klemm, G. Schreiber, M. Knapp, and R. Kužel, J. Appl. Crystallogr. **37**, 613 (2004).

[34] C. M. Huntington, J. L. Belof, K. J. M. Blobaum, R. M. Cavallo, N. B. Kostinski, B. R. Maddox, H.-S. Park, C. Plechaty, S. T. Prisbrey, R. Rudd, D. W. Swift, R. J. Wallace, S. V. Weber, C. Wehrenberg, M. J. Wilson, and B. A. Remington, in *Shock Compression of Condensed Matter - 2015: Proceedings of the Conference of the American Physical Society Topical Group on Shock Compression of Condensed Matter*, AIP Conf. Proc. No. 1793 (AIP, Melville, NY, 2017), p. 110007.

[35] N. Amadou, T. de Resseguier, A. Dragon, and E. Brambrink, Phys. Rev. B **98**, 024104 (2018).

[36] A. Stukowski, Modell. Simul. Mater. Sci. Eng. **18**, 015012 (2009).

[37] S. Martin, C. Ullrich, D. Šimek, U. Martin, and D. Rafaja, J. Appl. Crystallogr. **44**, 779 (2011).

[38] A. Stukowski and K. Albe, Modell. Simul. Mater. Sci. Eng. **18**, 085001 (2010).

[39] L. C. Chhabildas and J. R. Asay, J. Appl. Phys. **50**, 2749 (1979).

[40] D. Kalantar, G. Collins, J. Colvin, J. Eggert, J. Hawreliak, H. Lorenzana, M. Meyers, R. Minich, K. Rosolankova, M. Schneider, J. Stölken, and J. Wark, Int. J. Impact Eng. **33**, 343 (2006).

[41] A. Dewaele, C. Denoual, S. Anzellini, F. Occelli, M. Mezouar, P. Cordier, S. Merkel, M. Véron, and E. Rausch, Phys. Rev. B **91**, 174105 (2015).

[42] S. J. Wang, M. L. Sui, Y. T. Chen, Q. H. Lu, E. Ma, X. Y. Pei, Q. Z. Li, and H. B. Hu, Sci. Rep. **3**, 1086 (2013).

[43] N. Gunkelmann, D. R. Tramontina, E. M. Bringa, and H. M. Urbassek, J. Appl. Phys. **117**, 085901 (2015).